



Radio Observations of Four Active Galactic Nuclei Hosting Intermediate-mass Black Hole Candidates: Studying the Outflow Activity

Downloaded from: <https://research.chalmers.se>, 2024-04-25 14:28 UTC

Citation for the original published paper (version of record):

Yang, X., Mohan, P., Yang, J. et al (2022). Radio Observations of Four Active Galactic Nuclei Hosting Intermediate-mass Black Hole Candidates: Studying the Outflow Activity and Evolution. *Astrophysical Journal*, 941(1).
<http://dx.doi.org/10.3847/1538-4357/ac9e9d>

N.B. When citing this work, cite the original published paper.



Radio Observations of Four Active Galactic Nuclei Hosting Intermediate-mass Black Hole Candidates: Studying the Outflow Activity and Evolution

Xiaolong Yang^{1,2} , Prashanth Mohan¹ , Jun Yang³ , Luis C. Ho^{4,5} , J. N. H. S. Aditya^{6,7} , Shaohua Zhang⁸ ,
Sumit Jaiswal¹ , and Xiaofeng Yang⁹

¹ Shanghai Astronomical Observatory, Key Laboratory of Radio Astronomy, Chinese Academy of Sciences, Shanghai 200030, People's Republic of China
yangxl@shao.ac.cn

² Shanghai Key Laboratory of Space Navigation and Positioning Techniques, Shanghai Astronomical Observatory, Chinese Academy of Sciences, Shanghai 200030, People's Republic of China

³ Department of Space, Earth and Environment, Chalmers University of Technology, Onsala Space Observatory, SE-439 92 Onsala, Sweden

⁴ Kavli Institute for Astronomy and Astrophysics, Peking University, Beijing 100871, People's Republic of China

⁵ Department of Astronomy, School of Physics, Peking University, Beijing 100871, People's Republic of China

⁶ ARC centre for Excellence for All-Sky Astrophysics in 3 Dimensions (ASTRO 3D), Australia

⁷ Sydney Institute for Astronomy, School of Physics A28, The University of Sydney, NSW 2006, Australia

⁸ Shanghai Key Lab for Astrophysics, Shanghai Normal University, Shanghai 200234, People's Republic of China

⁹ Xinjiang Astronomical Observatory, Key Laboratory of Radio Astronomy, Chinese Academy of Sciences, 150 Science 1-Street, 830011 Urumqi, People's Republic of China

Received 2022 June 6; revised 2022 October 26; accepted 2022 October 27; published 2022 December 12

Abstract

Observational searches for intermediate-mass black holes (IMBHs; 10^2 – $10^6 M_\odot$) include relatively isolated dwarf galaxies. For those that host active galactic nuclei (AGNs), the IMBH nature may be discerned through the accretion–jet activity. We present radio observations of four AGN-hosting dwarf galaxies, which potentially harbor IMBHs. Very large array (VLA) observations indicate steep spectra (indices of -0.63 to -1.05) between 1.4 and 9 GHz. However, a comparison with the 9 GHz in-band spectral index shows a steepening for GH047 and GH158 (implying older/relic emission) and flattening for GH106 and GH163 (implying recent activity). Overlapping emission regions in the VLA 1.4 GHz and our very long baseline array (VLBA) 1.5 GHz observations, and possibly symmetric pc-scale extensions, are consistent with recent activity in the latter two. Using the compact VLBA radio luminosity, X-ray luminosity (probing the accretion activity), and the black hole masses, all AGNs are found to lie on the empirical fundamental plane relation. The four AGNs are radio-quiet with relatively higher Eddington ratios (0.04–0.32) and resemble X-ray binaries during spectral state transitions that entail an outflow ejection. Furthermore, the radio to X-ray luminosity ratio $\log R_X$ of -3.9 to -5.6 in these four sources support the scenarios that include corona mass ejection from the accretion disk and wind activity. The growth to kpc-scales likely proceeds along a similar trajectory to young AGNs and peaked spectrum sources. These complex clues can thus aid in the detection and monitoring of IMBHs in the nearby universe.

Unified Astronomy Thesaurus concepts: [Intermediate-mass black holes \(816\)](#); [Dwarf galaxies \(416\)](#); [Radio sources \(1358\)](#); [Very long baseline interferometry \(1769\)](#); [Accretion \(14\)](#)

1. Introduction

Astrophysical black holes (BHs), which are inferred through their observational signatures, are currently classified into two categories based on their mass. First, stellar-mass BHs (3 – $100 M_\odot$) originate from the end stages of the evolution of massive stars (Mirabel 2017), which has been inferred from studies of X-ray binaries (XRBs; that can host a BH actively accreting from a companion star) in our galaxy. Second, supermassive BHs (SMBHs; $\geq 10^6 M_\odot$) are resident at the centers of most massive galaxies with bulges (Kormendy & Ho 2013), which have been mainly inferred through their role in the evolution of the host galaxy (i.e., through the correlations of the SMBH mass with the galactic bulge properties, including the dispersion velocity, luminosity, and mass). While there have been deductions of SMBH hosts through their observational signatures (accretion power and nuclear activity), even in the early universe (≤ 1 Gyr, Wu et al. 2015; Bañados et al. 2018;

An et al. 2020), the modes of growth to such large masses (10^6 – $10^{10} M_\odot$) remain debatable (see Volonteri 2010; Greene et al. 2020). Possibilities include mergers and accretion activity. If growing from stellar-mass seed BHs, then these scenarios would require extremely high accretion rates. Meanwhile, the presence of intermediate-mass BHs (IMBHs; 10^2 – $10^6 M_\odot$) can help to realize these scenarios more efficiently than the lower mass seed BHs, and can thus help in understanding SMBH formation and their influence on galaxy evolution (see Volonteri 2010; Mezcua 2017; Greene et al. 2020, and references therein).

The study of IMBHs is also important to many related fields (e.g., Mezcua 2017; Greene et al. 2020), which include understanding if IMBH systems follow a potential scale invariance of disk–jet activity (accretion, jet/outflow ejection; i.e., spanning from stellar to supermassive; e.g., Falcke & Biermann 1995; Merloni et al. 2003; Gültekin et al. 2014); their role in enabling and powering tidal disruption events (e.g., Stone & Metzger 2016; Chen & Shen 2018), including as wandering off-nuclear (in their host galaxy) sources (e.g., Takekawa et al. 2019; Reines et al. 2020; Natarajan 2021; Paynter et al. 2021); and as contributors to the gravitational wave background when involving mergers (e.g., Natarajan 2021).

Based on the expected formation and evolution scenarios, observational searches for IMBHs have typically focused on the following habitats: globular clusters (e.g., Gebhardt et al. 2005; Kızıltan et al. 2017; Wen et al. 2021; Pechetti et al. 2022), ultra/hyper-luminous X-ray sources (e.g., Webb et al. 2012; Pasham et al. 2015), and dwarf galaxies (e.g., Filippenko & Ho 2003; Greene & Ho 2004). Among them, dwarf galaxies have recently received increasing attention because a number of them host AGNs (e.g., Davis et al. 2022, and references therein), which allows the identification of IMBHs based on their accretion signatures. These dwarf galaxies have undergone few merger events in their evolutionary history, and therefore have not grown significantly since their birth (Greene et al. 2020). A large fraction of dwarf galaxies with masses 10^7 – $10^{10} M_\odot$ may then potentially host 10^4 – $10^6 M_\odot$ black holes (e.g., Greene & Ho 2004, 2007; Dong et al. 2012; Reines et al. 2013; Chilingarian et al. 2018; Liu et al. 2018; Mezcuca et al. 2018).

Radio properties may be quantified in terms of the radio-loudness parameter (e.g., Kellermann et al. 1989) for comparison to optical properties and are given by $\mathcal{R} \equiv 1.3 \times 10^5 L_{5\text{GHz}}/L_B$, where $L_{5\text{GHz}}$ and L_B are the 5 GHz and optical B -band (4400 Å) monochromatic luminosities, respectively. Synchrotron emission in radio-loud AGNs (RL-AGNs; $\mathcal{R} > 10$) ensues primarily from the acceleration of electrons to relativistic energies by physical processes involving a jet (collimated outflow; e.g., Blandford & Königl 1979; Blandford et al. 2019). The relativistic jet can span a wide range of physical scales (from less than a pc to a few hundreds of kpc) and are ubiquitous in RL-AGNs, while a large portion of AGNs are radio-quiet (RQ, $\mathcal{R} < 10$). The absence of a prominent jet in RQ-AGNs allows a wide range of physical mechanisms producing radio emission to be probed (e.g., Panessa et al. 2019, and references therein). These can include sub-relativistic wide-angled winds (e.g., Zakamska & Greene 2014; Nims et al. 2015; Wang et al. 2021), lower power jets (e.g., Yang et al. 2020b, 2021; Wang et al. 2021), free-free emission from photoionized gas in the circum-nuclear region (Baskin & Laor 2021), star-forming regions (e.g., Yang et al. 2021), and accretion disk–corona activity (e.g., Laor & Behar 2008; Raginski & Laor 2016; Inoue & Doi 2018; Yang et al. 2020c).

A pilot radio survey and study of low-mass AGNs with high accretion rates by Greene et al. (2006) indicates that a large portion of these sources are predominantly radio-quiet. They draw a comparison to Galactic X-ray binaries (XRBs), where the high soft X-ray spectral state is characterized by a prominent accretion disk emission, and a quenched radio emission (e.g., McClintock & Remillard 2006). For AGNs at high accretion rates, a similarity with XRBs (if physical phenomena are scale independent, e.g., Heinz & Sunyaev 2003) may possibly explain their exceptionally low radio-loudness. Indeed, Yang et al. (2020c) find that a large portion of AGNs accreting at high and super-Eddington rates (Eddington ratio $\lambda_{\text{Edd}} = L_{\text{bol}}/L_{\text{Edd}} \gtrsim 1$, where L_{bol} is the bolometric luminosity and L_{Edd} is the Eddington luminosity) tend to be radio-quiet, which confirms an inverse relationship between \mathcal{R} and λ_{Edd} (Ho 2002).

The origin of X-ray and radio emission from the vicinity of the compact central engine in XRBs (putatively from the accretion and jet components respectively) motivates an investigation of their dependence on the black hole mass (M_{BH}) through a disk–jet coupling (fundamental plane relation, Merloni et al. 2003). However, the relationship does not clearly

distinguish between the RL and RQ-AGN, where the dominant emission mechanisms may differ. This may contribute in part to the scatter in the fitting. Furthermore, Laor & Behar (2008) find that optically selected RQ-AGN from the Palomar-Green bright quasar survey (Schmidt & Green 1983) indicates a constant $\log R_X \approx -5$, independent of M_{BH} , where $R_X \equiv L_{5\text{GHz}}/L_X$ (L_X is the 2–10 keV X-ray luminosity). However, Gültekin et al. (2014) find that a sample of low-mass AGNs ($\leq 10^{6.3} M_\odot$) falls within the statistical scatter on the fundamental plane relation. Bariuan et al. (2022) employ a statistically viable sample of RL and RQ-AGNs with radio and X-ray measurements to address this problem. They find that scatter in the fit (involving coefficients of L_X , M_{BH} and normalization) for RQ-AGNs is consistent with the relationship of Merloni et al. (2003) but that for RL-AGNs largely diverges. The relationship can then be used as a test for IMBHs hosted by low-mass RQ-AGNs, including in dwarf galaxies. However, Greene et al. (2006), Gültekin et al. (2014) and Bariuan et al. (2022) employ arcsec-scale resolution Very Large Array (VLA) radio observations to investigate the properties of the low-mass and RQ-AGN and arrive at the above conclusions relating to the complex relations governing \mathcal{R} , λ_{Edd} , and M_{BH} .

Very Long Baseline Interferometry (VLBI) radio observations offer high angular resolutions (at the milli-arcsec scale), surpassing other imaging techniques in astronomy. The VLBI detection of compact pc-scale radio-emitting structures (core/core-jet/jet-knot) in the nuclear regions of dwarf galaxies can directly probe the jet/outflow activity enabled by an accreting, potential IMBH. To date, high-resolution VLBI observational studies are limited to only individual IMBH candidate hosts: NGC 4395 (Wrobel & Ho 2006), Henize 2–10 (Reines & Deller 2012), NGC 404 (Paragi et al. 2014), RGG 9 (Yang et al. 2020a), and two recently observed sources NGC 4293 (Yang et al. 2022a) and RX J1301.9+2747 (Yang et al. 2022b). Observations of NGC 4395 ($R_X = -5$, Terashima & Wilson 2003) with the High Sensitivity Array (HSA) at 1.4 GHz reveal a radio-quiet nucleus and an elongated sub-pc scale structure, which is indicative of an outflow (Wrobel & Ho 2006). The recent study of NGC 4395 by Yang et al. (2022c) finds an undetected source from European VLBI Network (EVN) 5 GHz high-resolution observations. Very large array (VLA) 15 GHz observations detect a core (coincident with the Gaia optical position) and eastern (E) components. meanwhile, a new HSA imaging confirms the E component that is interpreted as a propagating shock originating from episodic ejection or outflow activity. Observations of NGC 404 with the EVN at 5 GHz (Paragi et al. 2014) results in a non-detection (sub-pc to pc scale), though extended structures over tens of pc have been detected by VLA 1.4 GHz observations (Nyland et al. 2012). A contemporaneous Chandra X-ray observation indicates a non-variable source with $\log R_X < -3.8$.

In this work, we present and discuss Very Long Baseline Array (VLBA) observational results from four IMBH candidates with masses $\sim 10^5 M_\odot$ (see Table 1). Throughout this work, we adopt the standard Λ CDM cosmology with a Hubble constant $H_0 = 70 \text{ km s}^{-1} \text{ Mpc}^{-1}$, and matter density and dark energy density parameters $\Omega_\Lambda = 0.73$, $\Omega_m = 0.27$, respectively.

2. The Sample

Greene & Ho (2004) identified 19 IMBH candidates from the Sloan Digital Sky Survey (SDSS) Data Release 1 (DR1). The virial mass technique has subsequently been used to

Table 1
IMBH Candidates Involved in Our Observational Campaign

Alias	SDSS	z	$\log M_{\text{BH}}$ (M_{\odot})	$\log L_{\text{X}(2-10\text{keV})}$ (erg s^{-1})	$\log L_{\text{H}\alpha}$ (erg s^{-1})	$\log L_{\text{B}}$ (erg s^{-1})	$\log \lambda_{\text{Edd}}$	$\log \mathcal{R}$	$\log R_{\text{X}}$
(1)	(2)	(3)	(4)	(5)	(6)	(7)	(8)	(9)	(10)
GH047	J082443.28+295923.5	0.025	5.6 [†]	42.4 ^a , 42.5 ^b	40.3	41.9	−0.8	−0.01	−5.6
GH106	J110501.98+594103.5	0.033	5.5 [†]	42.1 ^a	40.5	42.1	−0.5	0.85	−4.2
GH158	J131659.37+035319.9	0.045	5.8 [†]	41.7 ^a	40.6	42.2	−0.7	0.71	−3.9
GH163	J132428.24+044629.6	0.021	5.7 [†] , 5.8 [*]	41.7 ^a	39.7	41.4	−1.4	0.80	−4.6

Note. Columns give (1) identification from Greene & Ho (2007), (2) SDSS name, (3) redshift, (4) black hole mass (5) X-ray luminosity, (6) H α line luminosity, obtained from papers where black hole masses were measured, (7) B-band luminosity, estimated from H α line luminosity (see Greene & Ho 2007; Dong et al. 2012; Yang et al. 2020c), and (8–10) Eddington ratio, radio-loudness and radio to X-ray luminosity ratio, which are defined as $\lambda_{\text{Edd}} \equiv L_{\text{bol}}/L_{\text{Edd}}$, $\mathcal{R} \equiv 1.3 \times 10^5 L_{5\text{GHz}}/L_{\text{B}}$ and $R_{\text{X}} \equiv L_{5\text{GHz}}/L_{\text{X}}$, respectively, where $L_{\text{bol}} = 10L_{\text{B}}$ and $L_{\text{Edd}} = 1.26 \times 10^{38} (M_{\text{BH}}/M_{\odot})$ (erg s^{-1}) (see also Yang et al. 2020c). Here, we take 5 GHz luminosity estimated from VLBA L-band (see Table 4).

References for black hole mass. †: Greene & Ho (2007); *: Dong et al. (2012).

References for X-ray luminosity. a: Gültekin et al. (2014); b: Corral et al. (2014);

Table 2
VLBA L-band Observational Logs

Project ID	Target	Calibrator	Distance	Date	Antennas
BA146A ^a	GH047	J082341.1+292828	0.56	2021-5-31	SC-HN-NL-FD-LA-PT-KP-OV-BR-MK
BA146B ^b	GH106	J111013.0+602842	1.02	2021-6-1	SC-HN-NL-FD-LA-PT-KP-OV-BR-MK
BA146F ^b	GH158	J131829.6+043010	0.72	2021-7-10	SC-HN-FD-LA-PT-OV-BR-MK
BA146C ^c	GH163	J132626.6+032627	1.42	2021-7-2	SC-HN-FD-LA-PT-OV-BR-MK

Note. Columns give (1) project id, (2) target alias, (3) International Celestial Reference Frame (ICRF) name of the calibrator, (4) calibrator’s angular distance to the target (in degree), (5) date of the observation, and (6) participating antennas.

Operators. a: Jessica King, b: Alan Kerr, c: Betty Ragan.

Full names of the antennas. SC: St. Croix, HN: Hancock, NL: North Liberty, FD: Fort Davis, LA: Los Alamos, PT: Pie Town, KP: Kitt Peak, OV: Owens Valley, BR: Brewster, and MK: Maunakea.

identify several hundred IMBH candidates (Greene & Ho 2007; Dong et al. 2012; Reines et al. 2013; Liu et al. 2018) from the later SDSS data release. We compiled a list containing all targets (598 in total) from these studies, and then cross-matched it with the NRAO VLA Sky Survey (NVSS, Condon et al. 1998) and Faint Images of the Radio Sky at Twenty centimeters (FIRST, Becker et al. 1995) catalogs within 1'' of their optical positions. We found that 36 sources (6%) have radio counterparts (with signal-to-noise ratio >9) in the FIRST survey. Not surprisingly, NGC 4395 (Wrobel & Ho 2006) and RGG 9 (Yang et al. 2020a) are among these sources but are excluded from the present sample because they have already been observed in VLBI. We further made a selection using the following criteria: (1) an estimated black hole mass from literature of $<10^6 M_{\odot}$, (2) a FIRST radio flux density >2 mJy (signal-to-noise ratio >12), (3) sources which are X-ray detected, providing additional support for the presence of an AGN. Finally, four sources satisfy our selection criteria, see Table 1 for their main properties. The IMBH candidates in our sample are RQ-AGN ($\mathcal{R} < 10$) with $\log R_{\text{X}}$ in the range -5.6 to -3.9 and Eddington ratios $\log \lambda_{\text{Edd}}$ in the range -1.4 to -0.5 (sub-Eddington accretion sources).

3. Observation and Data Reduction

The VLBA observations were conducted from 2021 May 31 to July 10 (UT) under the project BA146 (see Table 2 for more information). The observations were scheduled at L-band (the central frequency is 1.545 GHz, hereafter we will use 1.5 GHz, in short), with a total observation time of 12 hr and a data recording rate of 2 Gbits per second. Phase-referencing mode

was used, and a nearby ($<2^{\circ}$) compact and strong radio source was chosen as a phase-reference calibrator for each target (see Table 2). The correlated data were processed using the Astronomical Image Processing System (AIPS, Greisen 2003) that was developed by the National Radio Astronomy Observatory (NRAO) of the USA. A priori amplitude calibration was performed using the system temperatures and antenna gain curves provided by each VLBA station. The Earth orientation parameters were obtained and calibrated using the measurements from the US Naval Observatory database, and the ionospheric dispersive delays were corrected from a map of the total electron content provided by the Crustal Dynamics Data Information System (CDDIS) of NASA.¹⁰ The opacity and parallactic angles were also corrected using the auxiliary files attached to the data. The instrumental delay in the visibility phase was calibrated using a strong fringe-finder source. Finally, a global fringe fitting on the phase-reference calibrator was performed, taking the calibrator’s phase model to solve miscellaneous phase delays of the target.

The calibrated data of the targets were exported into DIFMAP (Shepherd 1997) for imaging and model fitting. The final images were created using natural weights, see the right-hand panel of Figure 1. Both GH047 and GH158 have the signal-to-noise ratio of ~ 8 in the full resolution VLBA 1.5 GHz images. We performed a uv-taper in DIFMAP to identify the detection in GH047 and GH158, see Figure 2, where GH158 shows a clear detection with signal-to-noise ratio

¹⁰ <https://cddis.nasa.gov>

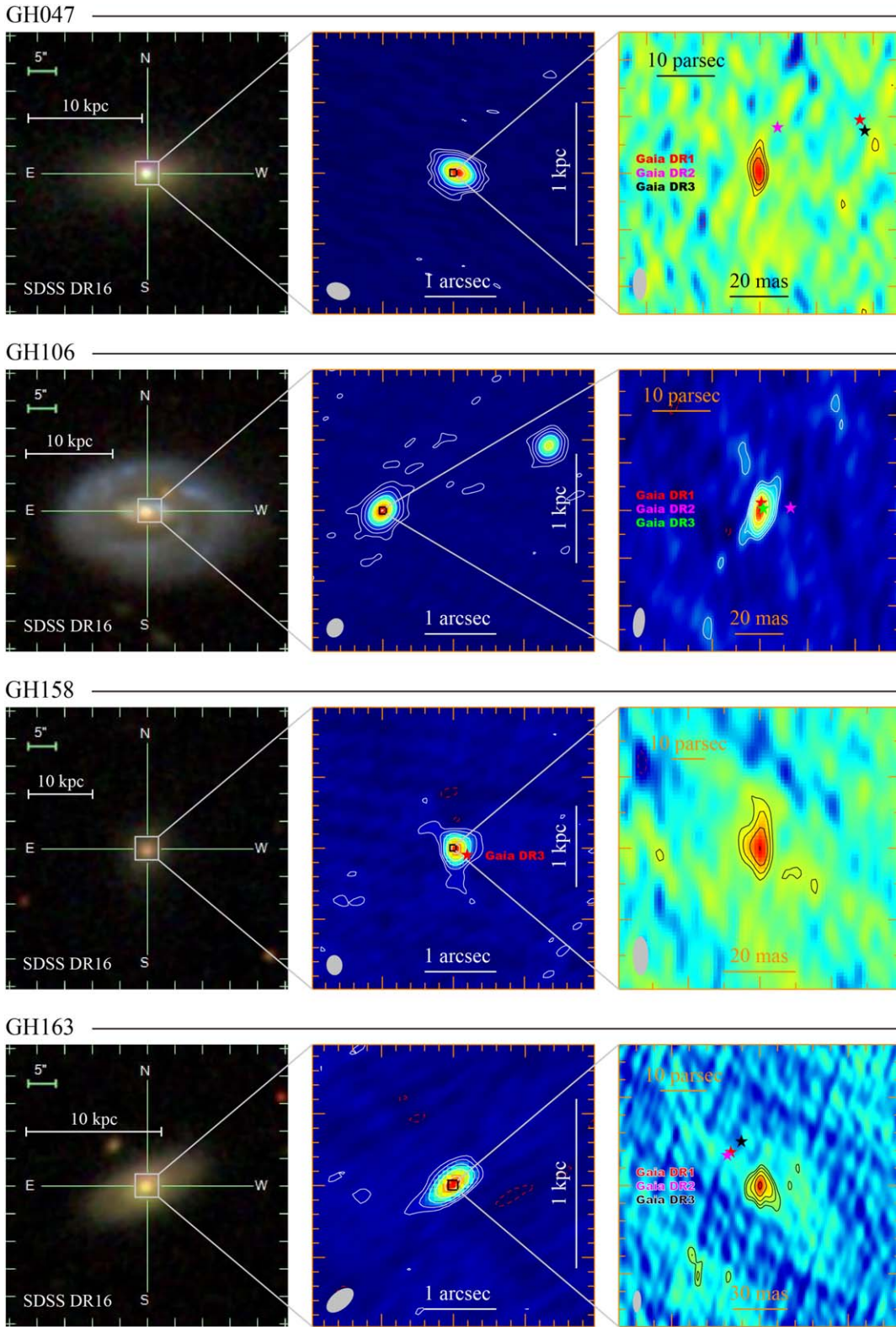


Figure 1. Multi-band images of the four IMBH candidates with core detected. Here the image matrix is collected as one source one line, where the left-hand column is from SDSS Data Release 16; the middle column is from VLA A-array X-band (9 GHz), and the right-hand column is from VLBA L-band (1.5 GHz). Each map is centered on the VLBA peak (see Table 3), except the VLA image of GH106. The black and white solid contours represent positive values and the red-dashed contours represent negative values. The contours are at $3\sigma \times (-1, 1, 2, 4, 8, \dots)$ for VLA images, while the contours are at $3\sigma \times (-1, 1, 1.41, 2, 2.83, \dots)$ for VLBA images. Here, 1σ noises are 0.016, 0.061, 0.031, 0.025 mJy beam⁻¹ for VLBA L-band images from the top to the bottom, respectively, and they equal the uncertainty of peak flux density (see Table 3) divided by 1.8 for VLA images. The gray ellipses in the bottom left-hand corner of each panel represent the full width at half-maximum (FWHM) of the restoring beam (see Table 3). Markers in the middle and right-hand column are the optical coordinates obtained from Gaia data release 1 (DR1), data release 2 (DR2) and data release 3 (DR3), where the astrometric uncertainty for Gaia is too small to be marked.

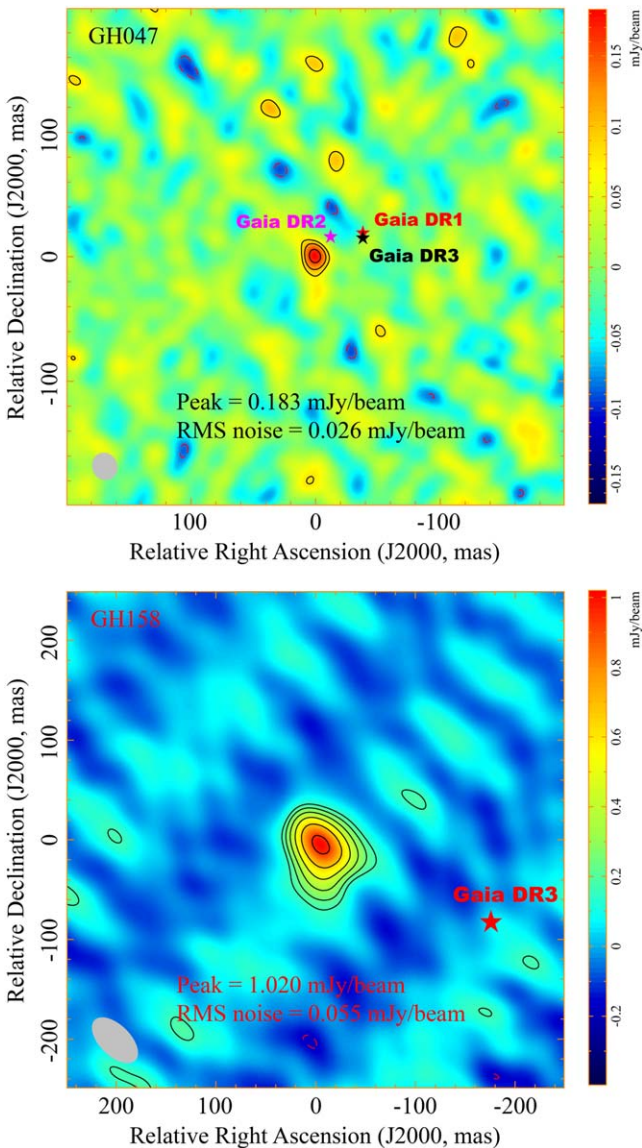


Figure 2. UV-tapered VLBA 1.5 GHz images of GH047 and GH158. The black solid contours represent positive values and the red-dashed contours represent negative values. The contours are at $3\sigma \times (-1, 1, 1.41, 2, 2.83, \dots)$. The peak flux densities and 1σ noises are marked in the images. The gray ellipses in the bottom left-hand corner of each panel represent the full width at half-maximum (FWHM) of the restoring beams, they are 22.4×20.1 (mas) at a position angle of $22^\circ 4'$ and 57.4×30.9 (mas) at a position angle of $45^\circ 2'$ for GH047 and GH158, respectively.

of 18, while GH047 still has a signal-to-noise ratio of ~ 7 and indicates a weak and compact radio emission.

For VLBA data, we estimate flux density uncertainties following the prescription of Fomalont (1999). The integrated flux densities S_i are extracted from Gaussian model-fit in DIFMAP with the task “MODELFIT”, where a standard deviation in model-fit is estimated for each component and is considered as the fitting noise error. Additionally, we assign a standard 5% error originating from amplitude calibration of VLBA (see VLBA Observational Status Summary 2021A¹¹).

We obtained VLA data of our targets from the NRAO archive, which were observed earlier under the two projects AG0777 (PI: Joan Wrobel; observed in 2008) and 12B-064

plus SD0129 (see Gültekin et al. 2014; observed from the end of 2012 to the beginning of 2013). No image has been published from any of the archival data, and hence we manually reduced the data using the Common Astronomy Software Application (CASA v5.1.1, McMullin et al. 2007) following the procedure described in Yang et al. (2020c). The model-fitting results of the VLA data are listed in Table 3. Here, the uncertainties on the integrated and peak flux density of the VLA data are estimated using the method described in Yang et al. (2020c).

4. Results

In the VLBA 1.5 GHz observations, all four sources are detected with a signal-to-noise ratio above 5σ . Figure 1 shows the SDSS DR16, the VLA A-array 9 GHz, and the VLBA 1.5 GHz images for each source (from left to right). The VLA A-array 1.4 and 9 GHz and VLBA 1.5 GHz observational results are listed in Table 3. The VLA A-array X-band observations used a wide-band filter with a bandwidth of 2 GHz (from 8 GHz to 10 GHz). The estimated in-band spectral indices between 8.5 and 9.5 GHz are listed in column 8 of Table 4.

In the VLA A-array X-band image of GH106, a nearby ($\sim 3''$ away from the core region, R.A. = $11^{\text{h}}05^{\text{m}}01^{\text{s}}.6734$, decl. = $59^\circ 41'04''.430$, J2000) radio source is detected in our data analysis (see Figure 1), which is located in the nuclear region of the host galaxy. The component has a 8.5–9.5 GHz in-band spectral index of -0.10 , which implies a flat spectrum. With limited sensitivity and resolution, VLA A-array L-band observations have only marginally detected the component, the VLA A-array L/X spectral index is -0.34 , which still implies a flat spectrum. The component is not detected in our VLBA L-band observations, and hence it is less compact than the nucleus. Based on the flat radio spectrum and the size, this component is possibly a ($<0''.3$ or <200 parsec in size) H II region (see e.g., Ulvestad & Antonucci 1997; Lacey et al. 1997).

At the VLBA mas-scales, all sources have compact emissions. The concentration indices (ratio of the peak S_p to integrated S_i flux densities) in Table 4 are indicative of GH047 and GH106 being relatively more compact than GH158 and GH163 at VLBA scales. Since the VLA L-band captures emissions from a larger area in comparison to the VLBA L-band observations, we can estimate the fraction of the extended emission for the AGN (from milli-arcsec to arcsec scales, see column 9 of Table 4). A major fraction ($\gtrsim 50\%$) of the emission is from extended scales in all AGN, which indicates that the VLBA observations tend to capture only the most compact emissions. Interestingly, GH047 tends to have a larger fraction of arcsec-scale radio emissions than the three other sources. We estimate the brightness temperature using (e.g., Ulvestad et al. 2005)

$$T_B = 1.8 \times 10^9 (1+z) \frac{S_i}{\nu^2 \phi^2} \text{ (K)}, \quad (1)$$

where S_i (mJy) are the integrated flux densities of each Gaussian component with a full width at half-maximum ϕ (mas). These parameters were estimated by fitting two-dimensional Gaussian models to the UV data. Meanwhile, ν is the observing frequency in GHz and z is the redshift. The measured flux densities S_i , FWHM of beam ϕ , and estimated brightness temperatures for the sources (at each observation frequency ν) are presented in Table 3. We note that the measured component sizes are upper limits, and therefore the

¹¹ <https://science.nrao.edu/facilities/vlba/docs/manuals/oss2021A>

Table 3
Observational Results

Name	Date	R.A. (J2000)	Decl. (J2000)	S_i (mJy)	S_p (mJy beam ⁻¹)	ϕ (mas)	$\theta_{b,maj}$ (mas)	$\theta_{b,min}$ (mas)	PA (degree)	$\log T_B$ (K)	$\log L_R$ (erg s ⁻¹)
(1)	(2)	(3)	(4)	(5)	(6)	(7)	(8)	(9)	(10)	(11)	(12)
VLBA <i>L</i> -band (1.5 GHz)											
GH047	2021-5-31	08:24:43.28793	+29:59:23.4978	0.185 ± 0.036	0.135 ± 0.017	4.23	11.4	4.8	-0.45	6.9	36.58 ± 0.08*
GH106	2021-6-1	11:05:01.98412	+59:41:03.5096	2.036 ± 0.131	1.460 ± 0.095	4.20	12.5	4.8	-6.59	7.9	38.39 ± 0.02*
GH158	2021-7-10	13:16:59.38357	+03:53:20.0327	0.750 ± 0.080	0.267 ± 0.033	8.62	10.8	4.3	0.61	6.9	38.23 ± 0.04*
GH163	2021-7-2	13:24:28.23767	+04:46:29.5448	0.836 ± 0.111	0.325 ± 0.029	9.35	12.4	4.6	-2.23	6.8	37.60 ± 0.05*
VLA A-array <i>L</i> -band (1.4 GHz)											
GH047	2008-12-1	08:24:43.278	+29:59:23.51	2.124 ± 0.127	2.020 ± 0.143	402	1850	1440	-84.6	4.0	38.16 ± 0.02◇
GH106	2008-12-5	11:05:01.998	+59:41:03.50	6.525 ± 0.492	4.100 ± 0.555	1133	1730	1450	-39.8	3.6	38.90 ± 0.03◇
GH158	2008-12-17	13:16:59.381	+03:53:20.04	1.855 ± 0.136	1.790 ± 0.154	56	1720	1530	11.2	5.7	38.62 ± 0.03◇
GH163	2008-12-17	13:24:28.241	+04:46:29.56	2.785 ± 0.211	2.570 ± 0.238	270	1740	1460	21.5	4.5	38.13 ± 0.03◇
VLA A-array <i>X</i> -band (9 GHz)											
GH047	2013-1-6	08:24:43.2837	+29:59:23.505	0.648 ± 0.010	0.664 ± 0.010	11.7	345	239	71.9	5.0	37.656 ± 0.006*
GH106	2012-11-15	11:05:01.9849	+59:41:03.507	0.918 ± 0.015	0.773 ± 0.014	102.5	282	231	-29.2	3.3	38.039 ± 0.007*
GH158	2012-12-15	13:16:59.3818	+03:53:20.025	0.398 ± 0.011	0.376 ± 0.012	58.9	282	225	4.02	3.4	37.967 ± 0.013*
GH163	2012-12-16	13:24:28.2385	+04:46:29.575	0.439 ± 0.011	0.401 ± 0.012	85.5	449	242	-50.6	3.1	37.325 ± 0.011*

Note. Columns give (1) source name, (2) date of the observation, (3–4) J2000 R.A. and decl. coordinates, (5) integrated flux density, (6) peak flux density, (7) FWHM size of Gaussian models, (8–10) FWHM size of beam major and minor axis, and position angle, (11) brightness temperature, and (12) monochromatic luminosity.

Monochromatic luminosity. *: estimated by taking the VLBA *L*-band radio flux density and the VLA A-array *L/X* spectral index; ◇: estimated by taking the VLA A-array *L*-band radio flux density and the VLA A-array *L/X* spectral index; •: estimated by taking the VLA A-array *X*-band radio flux density and the in-band VLA A-array wide *X*-band spectral index.

Table 4
Radio Observational Properties of the IMBH Candidates

Name	Telescope	ν (GHz)	R_{maj} (pc)	R_{min} (pc)	S_p/S_i	$\log L_{5\text{GHz}}$ (erg s ⁻¹)	α	fraction
(1)	(2)	(3)	(4)	(5)	(6)	(7)	(8)	(9)
GH047	VLBA	1.5	5.74	2.41	0.73 ± 0.19	$36.77 \pm 0.08^*$		
GH047	VLA-A	1.4	932	725	0.95 ± 0.09	$37.81 \pm 0.03^\diamond$	$-0.63 \pm 0.03^\ddagger$	0.90 ± 0.09
GH047	VLA-A	9	173	120	1.02 ± 0.02	$38.00 \pm 0.03^*$	$-1.38 \pm 0.13^\ddagger$	
GH106	VLBA	1.5	8.23	3.16	0.72 ± 0.06	$37.84 \pm 0.03^*$		
GH106	VLA-A	1.4	1140	955	0.63 ± 0.10	$38.32 \pm 0.03^\diamond$	$-1.05 \pm 0.04^\ddagger$	0.50 ± 0.15
GH106	VLA-A	9	185	152	0.84 ± 0.02	$38.10 \pm 0.04^*$	$-0.26 \pm 0.17^\ddagger$	
GH158	VLBA	1.5	9.56	3.80	0.36 ± 0.08	$37.80 \pm 0.05^*$		
GH158	VLA-A	1.4	1523	1355	0.96 ± 0.11	$38.17 \pm 0.03^\diamond$	$-0.82 \pm 0.04^\ddagger$	0.58 ± 0.10
GH158	VLA-A	9	249	199	0.94 ± 0.04	$38.26 \pm 0.08^*$	$-1.18 \pm 0.31^\ddagger$	
GH163	VLBA	1.5	5.27	1.95	0.39 ± 0.06	$37.09 \pm 0.06^*$		
GH163	VLA-A	1.4	739	620	0.92 ± 0.11	$37.58 \pm 0.03^\diamond$	$-0.99 \pm 0.04^\ddagger$	0.67 ± 0.11
GH163	VLA-A	9	190	102	0.91 ± 0.04	$37.46 \pm 0.06^*$	$-0.55 \pm 0.27^\ddagger$	

Note. Columns give (1) source alias, (2) telescope, (3) frequency, (4–5) major and minor axis of the beam, in physical scale (parsec), (6) the concentration index, (7) C-band (5 GHz) luminosity, (8) spectral index, and (9) the fraction of diffuse and extended radio emission between the compact VLA 1.4 GHz emission and the total VLBA 1.5 GHz emission over the compact VLA 1.4 GHz radio emission, defined as $\frac{S_{p,\text{VLA},1.4\text{GHz}} - S_i,\text{VLBA},1.5\text{GHz}}{S_{p,\text{VLA},1.4\text{GHz}}}$, here we assume the VLA 1.4 GHz and VLBA 1.5 GHz are at approximately equal frequency bands.

C-band Radio luminosity. $*$: estimated by taking the VLBA L -band radio flux density and the VLA A-array L/X spectral index; \diamond : estimated by taking the VLA A-array L -band radio flux density and the VLA A-array L/X spectral index; \bullet : estimated by taking the VLA A-array X -band radio flux density and the in-band VLA A-array wide X -band spectral index.

Radio spectral index. \ddagger : measured between VLA A-array L -band and X -band; \ddagger : the in-band spectral index obtained from the wide X -band spans from 8.5 to 9.5 GHz.

radio brightness temperatures estimated here should be considered as lower limits.

5. Discussion

5.1. The Fundamental Plane of Black Hole Activity

An empirical correlation among black hole mass, radio, and X-ray luminosity spanning XRBs (hosting stellar-mass black holes) and AGN (hosting SMBHs) is termed the fundamental plane relation of black hole activity (Merloni et al. 2003). This relation may be affected by radio emission produced in a jet/relativistic outflow, X-ray emission produced in a disk–corona system, and if both the radio and X-ray power are related to the black hole mass and accretion rate (see, e.g., Romero et al. 2017). Therefore, the fundamental plane relation may be applicable to any accretion-powered system during a low/hard state (Körding et al. 2006) or in an intermediate state that can involve the production of episodic/intermittent radio ejecta (Fender et al. 2004).

The validity of the fundamental plane relation for the current sample of potential IMBH hosting AGNs can be tested with the available X-ray and radio luminosities, and also with the measured black hole masses (see Table 1). The scatter in the relation can be contributed by the non-nuclear and extended radio emission (e.g., Saikia et al. 2018b). For the IMBH candidates in this work, the VLA-based radio flux densities at arcsec resolutions probe the kpc-scales, which can include contributions from the host galaxy. The radio emissions for the AGN components may thus be overestimated if we include the extended emission. Employing only the radio luminosity estimated from VLBA L -band flux densities, and the previously inferred X-ray luminosities and black hole masses (see Table 1), the IMBH candidate sample is found to closely follow the fundamental plane relation (see Figure 3). VLBA

observations of a sample of RQ-AGNs indicate that for sources with $\lambda_{\text{Edd}} \lesssim 0.3$, the radio emission originates from a compact region, potentially the size of the accretion disk (Alhosani et al. 2022); such a scenario may be operational in the current sample. For scale-independent physics, a similarity with XRB spectral state transitions places these IMBH sources in a high-soft state, characterized by a dominant accretion-based emission. The four sources in the sample have Eddington ratios of 0.04–0.32 (see Table 1) indicating a prominence of accretion-powered activity and the relative suppression of a radio-emitting jet (e.g., Gallo et al. 2003). The transition from a low-hard to a high-soft state involves the ejection of material (at relativistic velocities) that is likely to be responsible for the production of radio emission. The pc-scale outflow/jet may possibly be a signature of the above process and can be similar to the discrete ejection event observed in the IMBH candidate ESO 243-49 HLX-1 (Webb et al. 2012).

We include three additional low-luminosity AGNs, two of which are potential IMBH hosts. The availability of radio flux densities (and corresponding radio luminosity) from their pc-scale nuclear region, X-ray luminosities, and black hole mass estimates can be used to test their position on the fundamental plane relation, in an intermediate region (between the stellar-mass and supermassive scales) that is less populated. The sources include NGC 4395, NGC 404, and M32. For NGC 4395, the Eddington ratio is 1.2×10^{-3} (Wrobel & Ho 2006), and the black hole mass is $\approx 10^4 M_\odot$ (Woo et al. 2019). The 5 GHz radio luminosity of 1.3×10^{34} erg s⁻¹ is estimated from the VLA A array 15 GHz observations (Saikia et al. 2018a) which probes a region size of 4 pc (taking the in-band 15 GHz spectral index of -0.07 , see also Yang et al. 2022c), and the X-ray luminosity is $10^{39.9}$ erg s⁻¹ (Moran et al. 2005). For NGC 404, the Eddington ratio is 1.5×10^{-6} (Paragi et al. 2014), and the black hole mass $\approx 5 \times 10^5 M_\odot$ (Davis et al. 2020). The radio

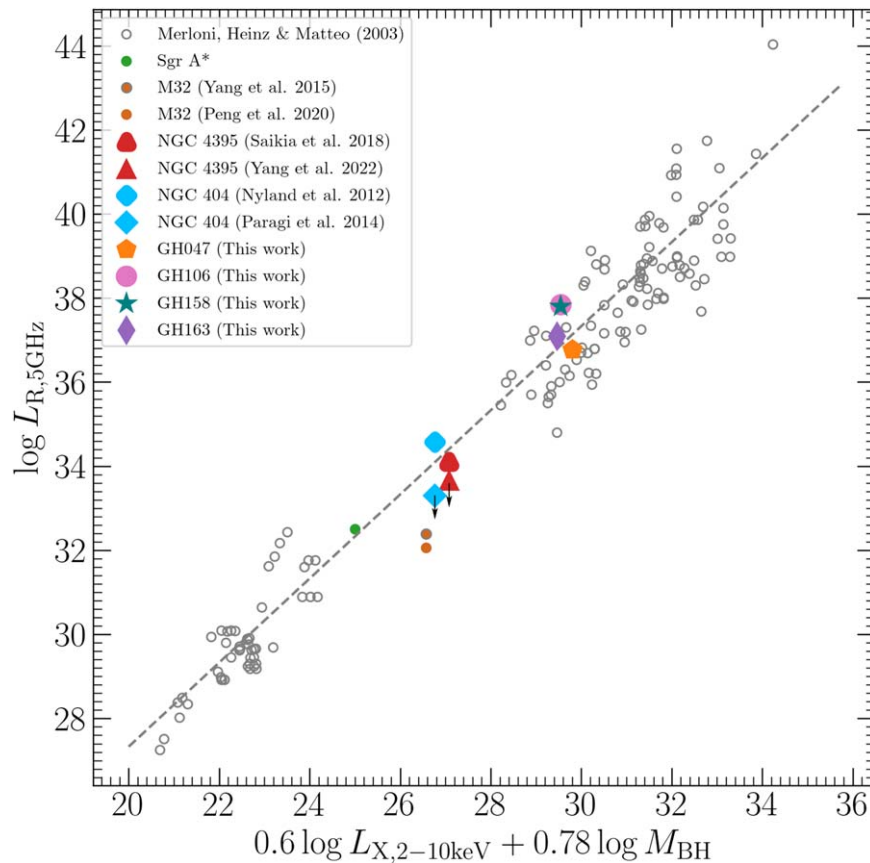


Figure 3. The fundamental plane of black hole activity based on Merloni et al. (2003). The references in the legend show where the radio luminosity was taken. The black open squares and data for Sgr A* are from Merloni et al. (2003). Note that the sub-parsec-scale radio luminosity (obtained from EVN observations) for NGC 4395 (Yang et al. In preparation) and NGC 404 (Paragi et al. 2014) are only upper limits.

luminosity is $3.2 \times 10^{34} \text{ erg s}^{-1}$ based on the VLA A array 5 GHz observations (Nyland et al. 2012) and $<2 \times 10^{33} \text{ erg s}^{-1}$ based on EVN 5 GHz observations (Paragi et al. 2014) that probe the sub-pc to pc scale region, and the X-ray luminosity is $1.4 \times 10^{37} \text{ erg s}^{-1}$ based on Chandra observations (Paragi et al. 2014). The source M32 is included here despite having a black hole mass of $\approx 3 \times 10^6 M_{\odot}$, mainly owing to a low Eddington ratio of $\approx 3.2 \times 10^{-9}$ (Ho et al. 2003). The radio luminosity is $2.5 \times 10^{32} \text{ erg s}^{-1}$ based on VLA B array 6.6 GHz observations (Yang et al. 2015) and $10^{32} \text{ erg s}^{-1}$ based on VLA A array 6 GHz observations (Peng et al. 2020) that probe regions of size $\approx 4 \text{ pc}$ and $\approx 1.5 \text{ pc}$, respectively. The X-ray luminosity is $7.9 \times 10^{35} \text{ erg s}^{-1}$ based on Chandra observations (Ho et al. 2003).

These sources are also found to follow the fundamental plane relation (see Figure 3). The low Eddington ratios ($\leq 10^{-5}$) for these sources are indicative of a radiatively inefficient mode of accretion onto the central black hole (e.g., Ho 2008, 2009; Yuan & Narayan 2014). This accretion mode is found to generally characterize a large sample of RQ-AGNs that follow the fundamental plane relation (e.g., Bariuan et al. 2022). A major portion of the gravitational binding energy and angular momentum accrued by the accreting radiatively inefficient gas in the vicinity of the black hole can be transported by global winds or outflows (e.g., Blandford & Begelman 1999; di Matteo et al. 2000; Ho 2008). The fundamental plane relation thus captures this activity regime and is indicative of a low-hard spectral state if similar to the XRBs (e.g., Falcke et al. 2004). A moderate resolution (corresponding to physical scales of a few

pc) and high sensitivity VLA (for nearby sources, for example, NGC 4395, NGC 404, and M32) or VLBI observation (for sources in this work) can thus help to capture the outflow/ejection activity of the central engine in the hard to the intermediate spectral regime.

5.2. The Nature of Radio Emission

All four sources have steep radio spectra between VLA A-array L and X-band (between -0.63 to -1.05), and span angular scales between $\approx 0''.2$ and $2''$ (physical size of tens of pc to kpc, see Tables 3 and 4). Comparing the spectral indices as inferred from the VLA L/X band and only from the X-band (in-band), the spectra of GH047 and GH158 tend to become steeper while that of GH106 and GH163 tend to become flatter. This implies the prevalence of older/relic emissions in GH047 and GH158 compared to GH106 and GH163, where the emission is more recent. However, the concentration index of the VLA X-band emission exceeds or is comparable to that in the VLA L -band emission in all sources (see Table 4), which suggests the emergence of a new emission from a flat spectrum compact component at higher frequencies. The in-band indices in the X-band (8.5–9.5 GHz) probe regions of size $\approx 100 \text{ pc}$ indicate that the recent activity in GH106 and GH163 is from the compact scales. This picture is consistent with the coincidence of the radio emission peak positions in their VLA 9 GHz and VLBA 1.5 GHz images, and indicates an active pc-scale region (see Figure 1). However, with low signal-to-noise ratio ($\sim 4\text{--}6\sigma$), there are possibly emergent

outflow structures along the NW-SE direction in GH106 and E-W direction in GH163 (see Figure 1) that may allude to this picture. Again, the flat spectrum (in-band index of -0.26 ± 0.17 at 9 GHz) in GH106 indicates the prevalence of optically thick emission in the nuclear region.

The Gaia mission primarily aims to measure the spatial position (astrometry) and velocity information from Galactic stars through photometric and spectroscopic surveys (Gaia Collaboration et al. 2016a). The instrument is suitable for VLBI-like measurements of the astrometric information for background non-stellar sources, including AGNs that may be present in the field of view (e.g., Yang et al. 2019) with sub-mas astrometric uncertainties for bright sources (Gaia Collaboration et al. 2016b, 2018, 2021). The Gaia optical and VLBA L-band radio positions for GH047 and GH163 are offset by ≈ 20 –30 mas, those of GH106 are coincident, and those of GH158 is offset by $\sim 0''.15$ (see the marker in Figure 2 and VLA X-band image of Figure 1). An offset itself may be an indicator that the Gaia observations track the accretion activity while the VLBI observations track the outflow activity. The relatively smaller offset (≤ 20 mas) or near coincidence for GH106 and GH163 are in agreement with the accretion-outflow activity being more recent in these sources.

The radio emission in these sources at the compact sub-pc to pc scales may originate from corona mass ejection or winds from the accretion disk (e.g., Panessa et al. 2019; Yang et al. 2020c). This is indicated by the radio VLBI to X-ray luminosity ratio ($L_{5 \text{ GHz}}/L_{2-10 \text{ keV}}$) for the four sources that spans between 2.5×10^{-6} to 1.3×10^{-4} . This spans a regime that is similar to that in coronal active stars (Guedel & Benz 1993) effected in the presence of strong magnetic fields (e.g., re-connection events) that can produce coronal mass ejection (e.g., Laor & Behar 2008; Panessa et al. 2019).

The non-thermal nature of the large-scale radio emission, steep spectral indices (between the VLA L and X band observations), and morphology suggest an un-beamed extended emission region. Furthermore, the emission is attributable to the extended structure that dominates over that from the compact VLBI scales, as inferred from the measured flux densities. The growth of the pc-scale outflow to the large-scale structure may proceed through intermittent/episodic activity (e.g., Nyland et al. 2020) for a scenario similar to the XRBs (in the low-hard state or a transition from low-hard to high-soft X-ray spectral shape, e.g., Fender et al. 2009) as has been inferred from Section 5.1. A coupling of the outflow with the accretion activity entails an intermittent/episodic nature (e.g., Czerny et al. 2009). The kpc-scale morphology can be structured by emission from a past jet ejection (e.g., Czerny et al. 2009; Nyland et al. 2020), and follows a growth trajectory that is similar to young AGNs or peaked spectrum sources (e.g., An & Baan 2012; Coppejans et al. 2016; O’Dea & Saikia 2021). In this scenario, the radio power can increase (scaling with time as $\propto t^{2/5}$) governed only by adiabatic losses. Following this stage, synchrotron losses begin to dominate as the source grows to the kpc-scale with power flattening, both stages are accompanied by steep (index of ≈ -1.0) spectra (e.g., Kaiser & Best 2007; An & Baan 2012). This may explain the relative dominance of the extended scale emission over that from the pc-scale outflow.

Physical properties of the emitting region can then be estimated by modeling the synchrotron emission that ensues from electrons accelerated by the expanding shock. Assuming a power-law electron number density distribution $N(\gamma) = K\gamma^{-p}$,

where p is the index related to the optically thin spectral index α as $p = 1 - 2\alpha$, and K is the normalization, the optically thin flux density (integrated over the pitch angle) can be expressed in terms of the synchrotron emissivity j_ν (Chevalier 1998; Ghisellini 2013), as follows:

$$F_\nu = j_\nu \frac{4\pi R^3 f_V}{3D_L^2}, \quad (2)$$

In this expression, $f_V \leq 1$ is the volume filling factor in a spherical region of size R ; $D_L(z)$ is the redshift dependent distance to the source (e.g., Hogg 1999); and the emissivity j_ν is expressed in terms of the particle normalization K , magnetic field energy density in the region $U_B = B^2/(8\pi)$ (where B is the magnetic field strength), and the energy index ps (Equation (4.45), Ghisellini 2013), as follows:

$$j_\nu = \frac{3\sigma_T c K U_B}{16\pi^{3/2} \nu_L} \left(\frac{\nu}{\nu_L} \right)^{-(p-1)/2} f_j(p), \quad (3)$$

where $\sigma_T = 6.65 \times 10^{-25} \text{ cm}^2$ is the Thomson cross section for electrons, $c = 3.0 \times 10^{10} \text{ cm s}^{-1}$ is the speed of light, $\nu_L = eB/(2\pi m_e c)$ is the Larmor frequency (where $e = 4.80 \times 10^{-10} \text{ esu}$ is the unit electric charge and $m_e = 9.11 \times 10^{-28} \text{ g}$ is the electron mass), and $f_j(p)$ in Equation (4.46) of Ghisellini (2013). The emission is from a region of size R and a volume filling factor $f_V \leq 1$. The distance to the source $D_L(z)$ is given by using z from Table 1 and assuming a standard Λ CDM with the parameters given in Section 1. Assuming an equipartition of the total energy density between the particle kinetic energy and magnetic fields, we obtain the following relationship between the normalization K and the magnetic field strength B (Chevalier 1998; Anderson et al. 2020)

$$K = \frac{\epsilon_e B^2}{\epsilon_B 8\pi} (p-2) \frac{\gamma_{\min}^{p-2}}{m_e c^2}, \quad (4)$$

where ϵ_e and ϵ_B are microphysical parameters (in addition to p) and represent the fractions of the total energy density (of the shocked material) in the particle kinetic energy density and in the magnetic field, respectively, and $\gamma_{\min} \approx \left(\frac{p-2}{p-1} \right) \epsilon_e \left(\frac{m_p}{m_e} \right)$ (e.g., Gao et al. 2013) is the minimum Lorentz factor of injected electrons (where $m_p = 1.67 \times 10^{-24} \text{ g}$ is the proton mass). Equations (3)–(4) are used in the expression for the flux density in Equation (2). The resulting equation can be inverted to express the magnetic field strength in a parametric form

$$B = \left(\frac{128\pi^{3/2} e}{\sigma_T} \left(\frac{e}{2\pi m_e c} \right)^{-(p-1)/2} \right)^{2/(p+5)} \left(\frac{F_\nu D_L^2 \nu^{(p-1)/2}}{(\epsilon_e/\epsilon_B) f_V f_j(p) (p-2) \gamma_{\min}^{(p-2)} R^3} \right)^{2/(p+5)}. \quad (5)$$

The total energy in the region can be evaluated as

$$E = \frac{4\pi}{3} R^3 f_V \frac{U_B}{\epsilon_B} = \frac{f_V}{6\epsilon_B} B^2 R^3. \quad (6)$$

This basic framework is independent of IMBH mass, which makes it applicable to a range of compact object systems hosting intermittent/episodic or sustained outflow activity.

Table 5
Emission Properties of the Large Scale Region

Source	z	F_ν (mJy)	p	R (pc)	B (mG)	E ($\times 10^{53}$ erg)
GH047	0.025	0.104	2.3	33.8	0.13	0.05
GH106	0.033	2.425	3.0	350.2	0.06	12.14
GH158	0.045	0.065	2.6	50.4	0.12	1.26
GH163	0.021	0.215	3.0	47.7	0.12	1.15

Note. Columns are (1) source alias, (2) source redshift, taken from Table 1, (3) total flux density of the emitting region $F_\nu = S_i - S_p$ based on the reported VLA L -band flux densities in Tables 3, 4 electron energy index $p = 1 - 2\alpha$ where the spectral indices α are the estimates from the LX band data in Table 3, (5) emitting region size evaluated as $R = R_{\min, \text{VLA}}(1 - S_p/S_i) - R_{\min, \text{VLBA}}$, (6) magnetic field strength in the emitting region B , and (7) total energy in the emitting region, E .

The magnetic field strength B and minimum total energy E in the emitting region (resolved, extended) are evaluated for the potential IMBH hosts. The flux density is $F_\nu = S_i - S_p$, where the VLA L -band values for S_i and S_p are taken from Table 3. The region size R is evaluated based on a weighting involving the concentration index (see Table 4), with $R = R_{\min, \text{VLA}}(1 - S_p/S_i) - R_{\min, \text{VLBA}}$. The evaluated R range is between 33.8 pc (GH047) and 350.2 pc (GH106). This region is likely to span between the VLBA pc-scale and the VLA sub-kpc to kpc-scales. We use an observational frequency $\nu = 5.0$ GHz, a power-law index $p = 1 - 2\alpha$ (using the LX band spectral indices reported in Table 3), and the assumptions $f_V = 0.5$ and (ϵ_e, ϵ_B) of $(1/3, 1/3)$. The magnetic field strength B ranges between 0.06–0.13 mG, and the total energy ranges between 0.05 and 12.14×10^{53} erg. Note that both values range subject to the free parameters in the model. The input parameters and the above estimates are tabulated in Table 5. The B values are similar to the mG estimates for the kpc-scale radio cores of radio-intermediate AGNs (e.g., Silpa et al. 2021). Imaging the sources at lower frequencies and in polarization may potentially unravel faint emission structures, including kpc-scale lobes where μG magnetic field strengths are expected (e.g., Silpa et al. 2022).

6. Summary and Conclusions

The presence of AGNs in dwarf galaxies (relatively isolated, mostly secular evolution, Mezcuca 2017; Greene et al. 2020) provides an opportunity to study the accretion–jet/outflow activity powered by a potential IMBH central engine. Synchrotron emission can be produced by physical processes involving an outflow. The evolutionary phase in these AGN systems may be similar to that in XRBs (spectral state transitions), due to a possible scale invariance of the underlying physical processes.

These mechanisms of emission and evolution from a compact to a large scale (pc–kpc) structure are investigated through a set of radio observations spanning multiple resolutions (and physical scales) involving four potential IMBH hosting AGNs. This includes our VLBA L -band (1.4 GHz) high-resolution observations (milli-arcsecond scale; probing the few to tens of pc) that were conducted in 2021, and archival VLA A-array L and X -band (1.5 GHz and 9 GHz respectively) intermediate to larger resolution observations (sub-arcsec to arcsec scales; probing \approx hundred pc to kpc). At the VLA scales, the source is compact and unresolved, though

with a dominant emission. At the VLBA scales, the sources become marginally resolved to allow the discerning of extensions from the compact emission regions.

The validity of the empirical fundamental plane of black hole activity (Merloni et al. 2003) is tested for a sample of sources, including the four putative IMBH candidates and three additional low-luminosity (and/or intermediate-mass) AGNs. Since these sources span a wide range of observables (radio and X-ray luminosities, and BH mass), they can help to discern the role of accretion–jet activity in affecting the fundamental plane relation. By including only the pc-scale region contribution to the radio emission (probing an active or recent outflow), we find that all sources are accommodated on the relationships within the general scatter and populate a region that is intermediate to that occupied by the XRBs and AGNs (see Figure 3).

In comparison to the XRB spectral states, the IMBH candidates are likely in the high-soft state (accretion-dominated emission), which indicates that the outflow may have recently been ejected (from a low-hard outflow-dominated state or an intermediate state). The low-luminosity AGNs are likely in the low-hard state involving ongoing outflow activity. The fundamental plane relation may thus be capturing the outflow and ejecta activity spanning the low-hard state and a recent intermediate spectral state.

The radio emission from the compact pc-scales may be sourced as corona mass ejection or disk winds (e.g., Laor & Behar 2008; Panessa et al. 2019), as indicated by the relative strength of the radio luminosity in comparison with the X-ray luminosity (that spans the range of $\approx 10^{-6}$ – 10^{-4}), a regime similar to that in coronal active stars (Guedel & Benz 1993), and at high accretion rates (e.g., Yang et al. 2020c). An offset in the emission center between the radio VLBI and optical Gaia is indicative of the former tracking the outflow and the latter tracking the accretion. A relatively smaller offset (≤ 20 mas) or coincidence of the positions are indicative of the outflow recently being ejected.

The emission from the kpc-scales is found to dominate over that from the pc-scale, possibly from past episodic/intermittent ejections that follow a trajectory of growth similar to that in young AGN and peak spectrum sources (e.g., An & Baan 2012; O’Dea & Saikia 2021). In this scenario, the luminosity tends to increase with time and then reaches a plateau phase when the growing structure reaches the kpc-scale (e.g., Kaiser & Best 2007; An & Baan 2012). The resultant synchrotron emission from the intermediate scales of a few ten pc to kpc is modeled to estimate a magnetic field strength of 0.06–0.13 mG and total energy of 0.05 – 12.14×10^{53} erg. These point to a relatively less powerful central engine in the dwarf galaxies (radio emission in comparison with the optical and X-ray emission) when compared to AGNs powered by SMBHs, with potentially differing growth mechanisms of the large-scale structure.

High to moderate resolution VLBI observations can probe the sub-pc to the pc-scale region in nearby dwarf galaxies hosting AGNs. Since these putatively harbor IMBHs powering the central engine, their VLBI monitoring can help us to understand the onset and evolution of accretion–jet activity, bridging the divide between the XRBs hosting stellar-mass BHs and AGNs hosting SMBHs, and can play a complementary role in a multi-wavelength perspective.

This work is supported by the Shanghai Sailing Program (21YF1455300) and China Postdoctoral Science Foundation (2021M693267). X.L.Y. is thankful for the support from the National Science Foundation of China (12103076). L.C.H. is supported by the National Science Foundation of China (11721303, 11991052, 12011540375), China Manned Space Project (CMS-CSST-2021-A04), and the National Key R&D Program of China (2016YFA0400702). X.F.Y. is supported by the CAS Pioneer Hundred Talents Program. Scientific results from data presented in this publication are derived from the VLBA project BA146. The National Radio Astronomy Observatory is a facility of the National Science Foundation operated under cooperative agreement by Associated Universities, Inc. This work has made use of data from the Pan-STARRS1 Surveys (PS1) and the PS1 public science archive. This work has made use of data from the European Space Agency (ESA) mission Gaia (<https://www.cosmos.esa.int/gaia>) processed by the Gaia Data Processing and Analysis Consortium (DPAC, <https://www.cosmos.esa.int/web/gaia/dpac/consortium>).

ORCID iDs

Xiaolong Yang  <https://orcid.org/0000-0002-4439-5580>
 Prashanth Mohan  <https://orcid.org/0000-0002-2211-0660>
 Jun Yang  <https://orcid.org/0000-0002-2322-5232>
 Luis C. Ho  <https://orcid.org/0000-0001-6947-5846>
 J. N. H. S. Aditya  <https://orcid.org/0000-0002-0268-0375>
 Shaohua Zhang  <https://orcid.org/0000-0001-8485-2814>
 Sumit Jaiswal  <https://orcid.org/0000-0002-5125-695X>
 Xiaofeng Yang  <https://orcid.org/0000-0001-5323-0764>

References

- Alhosani, A., Gelfand, J. D., Zaw, I., et al. 2022, *ApJ*, 936, 73
- An, T., & Baan, W. A. 2012, *ApJ*, 760, 77
- An, T., Mohan, P., Zhang, Y., et al. 2020, *NatCo*, 11, 143
- Anderson, M. M., Mooley, K. P., Hallinan, G., et al. 2020, *ApJ*, 903, 116
- Bañados, E., Venemans, B. P., Mazzucchelli, C., et al. 2018, *Natur*, 553, 473
- Bariuan, L. G. C., Snios, B., Sobolewska, M., Siemiginowska, A., & Schwartz, D. A. 2022, *MNRAS*, 513, 4673
- Baskin, A., & Laor, A. 2021, *MNRAS*, 508, 680
- Becker, R. H., White, R. L., & Helfand, D. J. 1995, *ApJ*, 450, 559
- Blandford, R., Meier, D., & Readhead, A. 2019, *ARA&A*, 57, 467
- Blandford, R. D., & Begelman, M. C. 1999, *MNRAS*, 303, L1
- Blandford, R. D., & Königl, A. 1979, *ApJ*, 232, 34
- Chen, J.-H., & Shen, R.-F. 2018, *ApJ*, 867, 20
- Chevalier, R. A. 1998, *ApJ*, 499, 810
- Chilingarian, I. V., Katkov, I. Y., Zolotukhin, I. Y., et al. 2018, *ApJ*, 863, 1
- Condon, J. J., Cotton, W. D., Greisen, E. W., et al. 1998, *AJ*, 115, 1693
- Coppejans, R., Cseh, D., van Velzen, S., et al. 2016, *MNRAS*, 459, 2455
- Corral, A., Georgantopoulos, I., Watson, M. G., et al. 2014, *A&A*, 569, A71
- Czerny, B., Siemiginowska, A., Janiuk, A., Nikiel-Wroczyński, B., & Stawarz, Ł. 2009, *ApJ*, 698, 840
- Davis, F., Kaviraj, S., Hardcastle, M. J., et al. 2022, *MNRAS*, 511, 4109
- Davis, T. A., Nguyen, D. D., Seth, A. C., et al. 2020, *MNRAS*, 496, 4061
- di Matteo, T., Quataert, E., Allen, S. W., Narayan, R., & Fabian, A. C. 2000, *MNRAS*, 311, 507
- Dong, X.-B., Ho, L. C., Yuan, W., et al. 2012, *ApJ*, 755, 167
- Falcke, H., & Biermann, P. L. R. 1995, *A&A*, 293, 665
- Falcke, H., Körding, E., & Markoff, S. 2004, *A&A*, 414, 895
- Fender, R. P., Belloni, T. M., & Gallo, E. 2004, *MNRAS*, 355, 1105
- Fender, R. P., Homan, J., & Belloni, T. M. 2009, *MNRAS*, 396, 1370
- Filippenko, A. V., & Ho, L. C. 2003, *ApJL*, 588, L13
- Fomalont, E. B. 1999, in ASP Conf. Ser. 180, *Synthesis Imaging in Radio Astronomy II*, ed. G. B. Taylor, C. L. Carilli, & R. A. Perley (San Francisco, CA: ASP), 301
- Gaia Collaboration, Prusti, T., de Bruijne, J. H. J., et al. 2016a, *A&A*, 595, A1
- Gaia Collaboration, Brown, A. G. A., Vallenari, A., et al. 2016b, *A&A*, 595, A2
- Gaia Collaboration, Brown, A. G. A., Vallenari, A., et al. 2018, *A&A*, 616, A1
- Gaia Collaboration, Brown, A. G. A., Vallenari, A., et al. 2021, *A&A*, 649, A1
- Gallo, E., Fender, R. P., & Pooley, G. G. 2003, *MNRAS*, 344, 60
- Gao, H., Lei, W.-H., Zou, Y.-C., Wu, X.-F., & Zhang, B. 2013, *NewAR*, 57, 141
- Gebhardt, K., Rich, R. M., & Ho, L. C. 2005, *ApJ*, 634, 1093
- Ghisellini, G. 2013, *Radiative Processes in High Energy Astrophysics*, Vol. 873 (Cham: Springer)
- Greene, J. E., & Ho, L. C. 2004, *ApJ*, 610, 722
- Greene, J. E., & Ho, L. C. 2007, *ApJ*, 670, 92
- Greene, J. E., Ho, L. C., & Ulvestad, J. S. 2006, *ApJ*, 636, 56
- Greene, J. E., Strader, J., & Ho, L. C. 2020, *ARA&A*, 58, 257
- Greisen, E. W. 2003, in *Information Handling in Astronomy - Historical Vistas*, ed. A. Heck, Vol. 285 (Dordrecht: Kluwer), 109
- Guedel, M., & Benz, A. O. 1993, *ApJL*, 405, L63
- Gültekin, K., Cackett, E. M., King, A. L., Miller, J. M., & Pinkney, J. 2014, *ApJL*, 788, L22
- Heinz, S., & Sunyaev, R. A. 2003, *MNRAS*, 343, L59
- Ho, L. C. 2002, *ApJ*, 564, 120
- Ho, L. C. 2008, *ARA&A*, 46, 475
- Ho, L. C. 2009, *ApJ*, 699, 626
- Ho, L. C., Terashima, Y., & Ulvestad, J. S. 2003, *ApJ*, 589, 783
- Hogg, D. W. 1999, arXiv:astro-ph/9905116
- Inoue, Y., & Doi, A. 2018, *ApJ*, 869, 114
- Kaiser, C. R., & Best, P. N. 2007, *MNRAS*, 381, 1548
- Kellermann, K. I., Sramek, R., Schmidt, M., Shaffer, D. B., & Green, R. 1989, *AJ*, 98, 1195
- Kızıltan, B., Baumgardt, H., & Loeb, A. 2017, *Natur*, 542, 203
- Körding, E., Falcke, H., & Corbel, S. 2006, *A&A*, 456, 439
- Kormendy, J., & Ho, L. C. 2013, *ARA&A*, 51, 511
- Lacey, C., Duric, N., & Goss, W. M. 1997, *ApJS*, 109, 417
- Laor, A., & Behar, E. 2008, *MNRAS*, 390, 847
- Liu, H.-Y., Yuan, W., Dong, X.-B., Zhou, H., & Liu, W.-J. 2018, *ApJS*, 235, 40
- McClintock, J. E., & Remillard, R. A. 2006, in *Compact Stellar X-Ray Sources*, ed. W. Lewin & M. van der Klis, Vol. 39 (Cambridge: Cambridge Univ. Press), 157
- McMullin, J. P., Waters, B., Schiebel, D., Young, W., & Golap, K. 2007, in ASP Conf. Ser. 376, *Astronomical Data Analysis Software and Systems XVI*, ed. R. A. Shaw, F. Hill, & D. J. Bell (San Francisco, CA: ASP), 127
- Merloni, A., Heinz, S., & Di Matteo, T. 2003, *MNRAS*, 345, 1057
- Mezcua, M. 2017, *IJMPD*, 26, 1730021
- Mezcua, M., Civano, F., Marchesi, S., et al. 2018, *MNRAS*, 478, 2576
- Mirabel, F. 2017, *NewAR*, 78, 1
- Moran, E. C., Eracleous, M., Leighly, K. M., et al. 2005, *AJ*, 129, 2108
- Natarajan, P. 2021, *MNRAS*, 501, 1413
- Nims, J., Quataert, E., & Faucher-Giguère, C.-A. 2015, *MNRAS*, 447, 3612
- Nyland, K., Marvil, J., Wrobel, J. M., Young, L. M., & Zauderer, B. A. 2012, *ApJ*, 753, 103
- Nyland, K., Dong, D. Z., Patil, P., et al. 2020, *ApJ*, 905, 74
- O'Dea, C. P., & Saikia, D. J. 2021, *A&ARv*, 29, 3
- Panessa, F., Baldi, R. D., Laor, A., et al. 2019, *NatAs*, 3, 387
- Paragi, Z., Frey, S., Kaaret, P., et al. 2014, *ApJ*, 791, 2
- Pasham, D. R., Cenko, S. B., Zoghbi, A., et al. 2015, *ApJL*, 811, L11
- Paynter, J., Webster, R., & Thrane, E. 2021, *NatAs*, 5, 560
- Pechetti, R., Seth, A., Kamann, S., et al. 2022, *ApJ*, 924, 48
- Peng, S., Li, Z., Sjouwerman, L. O., et al. 2020, *ApJ*, 894, 61
- Raginski, I., & Laor, A. 2016, *MNRAS*, 459, 2082
- Reines, A. E., Condon, J. J., Darling, J., & Greene, J. E. 2020, *ApJ*, 888, 36
- Reines, A. E., & Deller, A. T. 2012, *ApJL*, 750, L24
- Reines, A. E., Greene, J. E., & Geha, M. 2013, *ApJ*, 775, 116
- Romero, G. E., Boettcher, M., Markoff, S., & Tavecchio, F. 2017, *SSRv*, 207, 5
- Saikia, P., Körding, E., Coppejans, D. L., et al. 2018a, *A&A*, 616, A152
- Saikia, P., Körding, E., & Dibi, S. 2018b, *MNRAS*, 477, 2119
- Schmidt, M., & Green, R. F. 1983, *ApJ*, 269, 352
- Shepherd, M. C. 1997, in ASP Conf. Ser. 125, *Astronomical Data Analysis Software and Systems VI*, ed. G. Hunt & H. Payne (San Francisco, CA: ASP), 77
- Silpa, S., Kharb, P., Harrison, C. M., et al. 2022, *MNRAS*, 513, 4208
- Silpa, S., Kharb, P., Harrison, C. M., et al. 2021, *MNRAS*, 507, 991
- Stone, N. C., & Metzger, B. D. 2016, *MNRAS*, 455, 859
- Takekawa, S., Oka, T., Iwata, Y., Tsujimoto, S., & Nomura, M. 2019, *ApJL*, 871, L1
- Terashima, Y., & Wilson, A. S. 2003, *ApJ*, 583, 145
- Ulvestad, J. S., & Antonucci, R. R. J. 1997, *ApJ*, 488, 621
- Ulvestad, J. S., Antonucci, R. R. J., & Barvainis, R. 2005, *ApJ*, 621, 123

- Volonteri, M. 2010, [A&ARv](#), **18**, 279
- Wang, A., An, T., Jaiswal, S., et al. 2021, [MNRAS](#), **504**, 3823
- Webb, N., Cseh, D., Lenc, E., et al. 2012, [Sci](#), **337**, 554
- Wen, S., Jonker, P. G., Stone, N. C., & Zabludoff, A. I. 2021, [ApJ](#), **918**, 46
- Woo, J.-H., Cho, H., Gallo, E., et al. 2019, [NatAs](#), **3**, 755
- Wrobel, J. M., & Ho, L. C. 2006, [ApJL](#), **646**, L95
- Wu, X.-B., Wang, F., Fan, X., et al. 2015, [Natur](#), **518**, 512
- Yang, J., An, T., Zheng, F., et al. 2019, [MNRAS](#), **482**, 1701
- Yang, J., Gurvits, L. I., Paragi, Z., et al. 2020a, [MNRAS](#), **495**, L71
- Yang, J., Paragi, Z., An, T., et al. 2020b, [MNRAS](#), **494**, 1744
- Yang, J., Paragi, Z., Nardini, E., et al. 2021, [MNRAS](#), **500**, 2620
- Yang, J., Yang, X., Wrobel, J. M., et al. 2022c, [MNRAS](#), **514**, 6215
- Yang, L., Shu, X., Zhang, F., et al. 2022b, [ApJ](#), **935**, 115
- Yang, X., Wang, R., & Guo, Q. 2022a, [MNRAS](#), **517**, 4
- Yang, X., Yao, S., Yang, J., et al. 2020c, [ApJ](#), **904**, 200
- Yang, Y., Li, Z., Sjouwerman, L. O., et al. 2015, [ApJL](#), **807**, L19
- Yuan, F., & Narayan, R. 2014, [ARA&A](#), **52**, 529
- Zakamska, N. L., & Greene, J. E. 2014, [MNRAS](#), **442**, 784